Migration behaviors of leaky dielectric droplets with electric and hydrodynamic forces

Yanning Wang,[1,2] Dongliang Sun,[1,*] Yinshi Li,[2,†] Shuai Chen,[1] and Bo Yu[1]

[1]*School of Mechanical Engineering, Beijing Institute of Petrochemical Technology, 19 Qingyuan North Rd., Beijing 102617, China*
[2]*Key Laboratory of Thermo-Fluid Science and Engineering of MOE, School of Energy and Power Engineering,*
Xi'an Jiaotong University, Xi'an, Shaanxi 710049, China

The external electric field enables separation and transport of droplets effectively in microfluidic devices. Herein, a volume-of-fluid (VOF) + level-set (LS) + smoothed physical parameters (SPP) method associated with the dynamically adaptive grid technique is extended to simulate three-dimensional leaky dielectric droplets in the electric field. The effects of electric and hydrodynamic forces on droplet behaviors are investigated. It is demonstrated that the electric force could act toward the outside or inside of a droplet and produce different droplet deformations. For the dielectrophoretic migration of droplets in the nonuniform electric field, the electric force has a dominant effect. It is found that when the electric conductivity ratio is greater than 1, an unbalanced electric force toward a stronger electric field is generated, bringing about the migration toward a stronger electric field. In contrast, when the electric conductivity ratio is smaller than 1, the unbalanced electric force direction is reversed and the droplet migrates toward a weaker electric field. The hydrodynamic force produces little promotion or hindrance to droplet migration. A greater permittivity ratio usually produces greater electric force and migration velocity. The droplet migrates along one direction in a symmetric nonuniform electric field but tends to migrate along the normal direction of electric potential profiles in an asymmetric nonuniform electric field.

I. INTRODUCTION

Electrohydrodynamics (EHD), which is an interdisciplinary field of hydrodynamics and electrodynamics, focuses on the interaction between fluids and electric fields. Once a two-phase flow system is subjected to an external electric field, the electric stress exerted on the fluid alters the fluid flow situation, and the electric field distribution is modified by fluid flow in return. Imposing an electric field has become a widespread technique to manipulate fluid flow and alter fluid behaviors in industrial applications [1–6]. Because droplets undergo deformation and dielectrophoretic migration at the same time under the action of electric force, it is efficient to control droplet transportation in microfluidic devices by electric fields [4,5].

A pioneering theoretical model, known as the leaky dielectric model, of droplet behavior in uniform electric fields was proposed by Taylor [7]. The theory is further extended to the prediction of transient droplet behaviors in uniform electric fields by solving the coupled flow and electric field equations [8,9]. The effectiveness of the leaky dielectric model for the prediction of small droplet deformation is validated [7,10–14]. More complicated and comprehensive investigations of droplet behavior in uniform electric fields have also been conducted by experimental and numerical simulation methodologies [15–19]. Lin *et al.* [15] applied the phase field model to the prediction of deformation and interior flow of a leaky dielectric droplet. Cui *et al.* [16] concluded that a prolate droplet may undergo periodic oscillation under certain circumstances. Salipante and Vlahovska [17] found that the droplets in a strong electric field might rotate and have oblique orientation. Breaking up of droplets along the electric field direction occurs when the electric field intensity is greater than a critical value [18,19].

Generally speaking, because the electric force exerted on droplets is perfectly symmetric, a single droplet in the appropriate electric field turns into an ellipsoid shape from a sphere but its position remains still. The interfacial electric stress around the droplet gives rise to the circulatory flow, and four identical vortices appear in the droplet [20,21]. To break the symmetry and lead to the dielectrophoretic migration of an uncharged droplet, application of a nonuniform electric field is inevitable.

Early research on droplet behaviors in nonuniform electric fields can be traced back to Feng [22], who compared the different behaviors of a fluid droplet and a solid sphere with different physical parameters and obtained the droplet dielectrophoretic velocity, after which detailed analyses of the deformation, motion, and breakup of droplets in nonuniform electric fields were carried out [23–29]. A perfect dielectric droplet might take the form of an oblate shape, which is in sharp contrast to droplets in a uniform electric field [23]. The circulatory flow inside a leaky dielectric droplet proved to be more intense than that in a uniform electric field [24]. Mandal *et al.* [25] generalized the theory of Feng [22] by taking the effects of surface charge convection and shape deformation into consideration. The gravitational field [26] and external flow field [27] were further coupled with the electric field

*Corresponding author: sundongliang@bipt.edu.cn
†Corresponding author: ysli@mail.xjtu.edu.cn

in their subsequent work. Some scholars [28,29] also investigated droplet dielectrophoretic migration and deformation in alternating current electric fields. Overall, the investigations of droplet dynamic behaviors in nonuniform electric fields are mainly concentrated on theoretical analyses, which are valid only for small droplet deformation and Stokes flow. The experimental and numerical investigations [24,30,31] are far from sufficient compared with the progress made regarding EHD in uniform electric fields.

Although implicit methods, such as the volume-of-fluid (VOF) and level-set (LS) methods, are convenient to deal with the topological changes of an interface, most of them have not been applied to the simulation of EHD flow in nonuniform electric fields. In this work, a VOF+LS+SPP (smoothed physical parameters) method [32,33], which is developed to predict the dynamic behaviors of perfect dielectric fluids, is extended to the simulation of three-dimensional leaky dielectric droplets in an electric field with the help of a dynamically adaptive grid technique. The accuracy of this method is verified by comparing with previous results. It is found that the flow field and electric force around the droplet in a uniform electric field have different distributions for different electric conductivities and permittivities. The symmetries of electric and hydrodynamic forces are broken by the nonuniform electric field and the unbalanced forces are produced, which has a significant influence on droplet behaviors. Meanwhile, the droplet deformation and dielectrophoretic migration in the symmetric and asymmetric nonuniform electric fields are investigated.

II. GOVERNING EQUATIONS AND NUMERICAL METHODS

A. Governing equations

Assuming the droplet and external fluid are incompressible Newtonian fluids and the fluid flow is laminar and unsteady, the continuity and momentum equations are

$$\nabla \cdot \boldsymbol{u} = 0, \tag{1}$$

$$\frac{\partial(\rho \boldsymbol{u})}{\partial t} + \nabla \cdot (\rho \boldsymbol{u}\boldsymbol{u}) = -\nabla p + \nabla \cdot [\mu(\nabla \boldsymbol{u} + \nabla \boldsymbol{u}^T)] + \rho \boldsymbol{g} + \boldsymbol{F}_\sigma + \boldsymbol{F}_e, \tag{2}$$

where $\boldsymbol{u}$ is the velocity vector, ρ is the density, t is the time, p is the pressure, μ is the dynamic viscosity, $\boldsymbol{g}$ is the gravitational acceleration, $\boldsymbol{F}_\sigma$ is the surface tension, and $\boldsymbol{F}_e$ is the electric force.

B. VOF+LS+SPP method

The VOF+LS+SPP method [32,33] is applied to deal with two-phase EHD flow. In the VOF method, a volume fraction α, which is the basis of constructing the phase interface, is defined to be the volume fraction for each phase in each grid cell. The evolution of volume fraction α satisfies

$$\alpha_i + \alpha_o = 1, \tag{3}$$

$$\frac{\partial \alpha_o}{\partial t} + \nabla \cdot (\boldsymbol{u}\alpha_o) = 0, \tag{4}$$

where the subscripts i and o refer to the fluid inside and outside of the droplet, respectively.

A LS function φ is defined to be the signed distance from the interface.

$$\varphi(\boldsymbol{r}, t) = \begin{cases} +|d| & \boldsymbol{r} \in \text{outside of the droplet} \\ 0 & \boldsymbol{r} \in \text{the interface} \\ -|d| & \boldsymbol{r} \in \text{inside of the droplet} \end{cases}, \tag{5}$$

where $\boldsymbol{r}$ is the position vector and d is the distance from the interface. The evolution of φ is given as

$$\frac{\partial \varphi}{\partial t} + \boldsymbol{u} \cdot \nabla \varphi = 0. \tag{6}$$

The SPP, including density ρ, dynamic viscosity μ, electric conductivity σ, and permittivity ε, are obtained by

$$\rho = \rho_i(1 - H(\varphi)) + \rho_o H(\varphi), \tag{7}$$

$$\mu = \mu_i(1 - H(\varphi)) + \mu_o H(\varphi), \tag{8}$$

$$\sigma = \sigma_i(1 - H(\varphi)) + \sigma_o H(\varphi), \tag{9}$$

$$\varepsilon = \varepsilon_i(1 - H(\varphi)) + \varepsilon_o H(\varphi), \tag{10}$$

where $H(\varphi)$ is the Heaviside function and is defined as

$$H(\varphi) = \begin{cases} 0 & \varphi < -a \\ \frac{1}{2}\left[1 + \frac{\varphi}{a} + \frac{1}{\pi}\sin\left(\frac{\pi\varphi}{a}\right)\right] & |\varphi| \leqslant a \\ 1 & \varphi > a \end{cases}, \tag{11}$$

where $a = 1.5\Delta$, and Δ denotes the grid size.

A continuum surface force (CSF) model [34] is utilized to calculate the surface tension $\boldsymbol{F}_\sigma$:

$$\boldsymbol{F}_\sigma = -\gamma \kappa(\varphi)\delta(\varphi)\nabla\varphi, \tag{12}$$

where γ is the surface tension coefficient, and

$$\kappa(\varphi) = \nabla \cdot \left(\frac{\nabla\varphi}{|\nabla\varphi|}\right), \tag{13}$$

$$\delta(\varphi) = \begin{cases} \frac{1+\cos(\pi\varphi/a)}{2a} & |\varphi| \leqslant a \\ 0 & |\varphi| > a \end{cases}. \tag{14}$$

C. Leaky dielectric model

For two leaky dielectric fluids, there exists a small amount of free charges throughout the whole space. It is reasonable to assume that the free charges accumulate at the interface much faster than the fluid motion [7], and the charge conservation equation is

$$\nabla \cdot (\sigma \boldsymbol{E}) = 0, \tag{15}$$

where $\boldsymbol{E}$ is the electric field intensity.

In EHD, the dynamic current is so small that the magnetic induction is neglected. According to Maxwell equations, the electric field intensity satisfies

$$\nabla \times \boldsymbol{E} = 0, \tag{16}$$

$$\nabla \cdot (\varepsilon_0 \varepsilon \boldsymbol{E}) = q, \tag{17}$$

where ε_0 is the permittivity of vacuum, and q is the volume density of local free charges.

According to Eq. (16), the electric field intensity can be expressed as the gradient of electric potential ϕ:

$$\boldsymbol{E} = -\boldsymbol{\nabla}\phi. \qquad (18)$$

Combining Eqs. (15) and (18), it can be obtained that

$$\boldsymbol{\nabla} \cdot (\sigma \boldsymbol{\nabla}\phi) = 0. \qquad (19)$$

The volume density of local free charges q is

$$q = \boldsymbol{\nabla} \cdot (\varepsilon_0 \varepsilon \boldsymbol{E}) = \sigma \boldsymbol{E} \cdot \boldsymbol{\nabla}\left(\frac{\varepsilon_0 \varepsilon}{\sigma}\right). \qquad (20)$$

The electric force is given by [20,21]

$$\boldsymbol{F}_e = q\boldsymbol{E} - \frac{1}{2}\varepsilon_0 \boldsymbol{E} \cdot \boldsymbol{E}\boldsymbol{\nabla}\varepsilon + \frac{1}{2}\varepsilon_0 \boldsymbol{\nabla}\left(\rho\boldsymbol{E} \cdot \boldsymbol{E}\frac{\partial\varepsilon}{\partial\rho}\right). \qquad (21)$$

The first term is the Coulomb force which acts along the direction of the electric field due to free charges. The second term is the dielectric force which acts perpendicularly to the interface due to polarization charges. The third term is the electrostrictive force which is caused by inhomogeneity of the electric field and variation of permittivity with density. The electrostrictive force is ignored for incompressible fluids [12].

D. Solving methodology

The velocity and pressure [Eqs. (1) and (2)] are coupled by the PISO algorithm. The second-order upwind scheme is utilized to discretize the convection term in the momentum and LS equations [Eqs. (2) and (6)]. The user-defined scalar electric potential is introduced to solve Eq. (19). The user-defined functions are developed to calculate the electric force [Eq. (21)] and SPP [Eqs. (7)–(10)]. The geometric reconstruction scheme [35] is adopted to solve the volume fraction equation [Eq. (4)]. The first-order implicit scheme treats the time marching. The Courant number Co is defined to control the time step Δt by setting Co $\leqslant 0.01$:

$$\text{Co} = \frac{\Delta t}{\Delta/|\boldsymbol{u}|}. \qquad (22)$$

III. DROPLET IN THE UNIFORM ELECTRIC FIELD

A. Physical problem

A spherical droplet with a radius R is located in the center of a cubic cavity, as shown in Fig. 1(a). A uniform electric
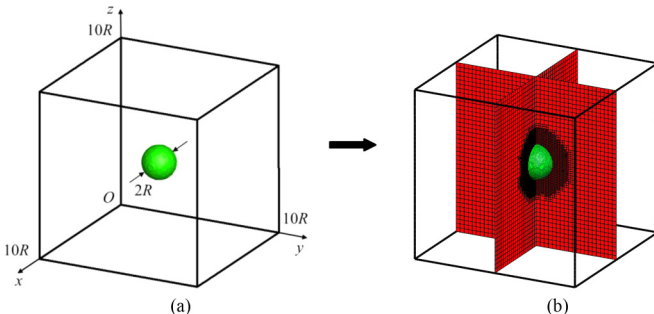

FIG. 1. Physical problem of droplet deformation in the electric field: (a) schematic diagram and (b) grid system.

field, along the vertical direction with a magnitude of $E_0 = \phi_0/10R$, is generated by an applied voltage between the top and bottom plates. The boundary conditions are listed below:

$$\begin{aligned}
&z = 10R, \quad \text{no-slip wall}, \quad \phi = \phi_0 \\
&z = 0, \quad \text{no-slip wall}, \quad \phi = 0 \\
&x = 10R, \quad \text{no-slip wall}, \quad \frac{d\phi}{dn} = 0 \\
&x = 0, \quad \text{no-slip wall}, \quad \frac{d\phi}{dn} = 0 \\
&y = 10R, \quad \text{no-slip wall}, \quad \frac{d\phi}{dn} = 0 \\
&y = 0, \quad \text{no-slip wall}, \quad \frac{d\phi}{dn} = 0.
\end{aligned} \qquad (23)$$

The grid number required for a full three-dimensional EHD problem increases dramatically compared with the simulation of a two-dimensional problem [32,33]. The dynamically adaptive grid technique is introduced to refine the grids near the interface and save computer resources. In Fig. 1(b), the base grid is $40 \times 40 \times 40$, three grid levels are applied, and the grid resolution R/Δ increases from 4 to 16. The grid number is only 219 022, while the grid number of a uniform grid system needs to be 4 096 000 to keep the same resolution. The region using the dynamically adaptive grid technique is confined by

$$|\varphi| \leqslant R. \qquad (24)$$

The densities of two fluids are assumed to be identical. The behaviors of a leaky dielectric droplet in the electric field are characterized by four dimensionless parameters:

$$\lambda_\sigma = \frac{\sigma_i}{\sigma_o}, \quad \lambda_\varepsilon = \frac{\varepsilon_i}{\varepsilon_o}, \quad \lambda_\mu = \frac{\mu_i}{\mu_o}, \quad \text{Ca}_E = \frac{\varepsilon_0 \varepsilon_o E_0^2 R}{\gamma}, \qquad (25)$$

where λ_σ, λ_ε, and λ_μ are the ratios of electric conductivity, permittivity, and dynamic viscosity between the droplet and external fluid, respectively. The electric capillary number Ca_E describes the relative importance of electric force and surface tension.

A spherical leaky dielectric droplet surrounded by another leaky dielectric fluid deforms into either a prolate ellipsoid ($D > 0$) or an oblate ellipsoid ($D < 0$) in the electric field, as shown in Fig. 2. The deformation rate D is defined as

$$D = \frac{L - B}{L + B}, \qquad (26)$$

where L and B are the maximum droplet length along the parallel and vertical direction of the electric field, respectively.

Under the assumption of Stokes flow, Taylor [7] presented that the terminal deformation rate of a leaky dielectric droplet in the electric field is

$$D = \frac{9f_d(\lambda_\sigma, \lambda_\varepsilon, \lambda_\mu)}{16(2 + \lambda_\sigma)^2}\text{Ca}_E,$$

$$f_d(\lambda_\sigma, \lambda_\varepsilon, \lambda_\mu) = \lambda_\sigma^2 + 1 - 2\lambda_\varepsilon + \frac{3}{5}(\lambda_\sigma - \lambda_\varepsilon)\frac{2 + 3\lambda_\mu}{1 + \lambda_\mu}. \qquad (27)$$
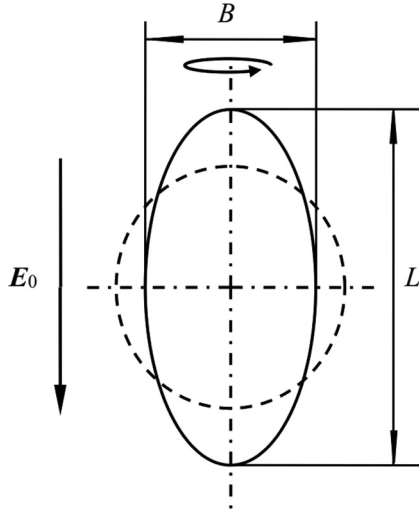
FIG. 2. Schematic of droplet deformation.

When $f_d(\lambda_\sigma, \lambda_\varepsilon, \lambda_\mu) = 0$, the droplet still remains spherical. The droplet takes the form of a prolate ellipsoid when $f_d(\lambda_\sigma, \lambda_\varepsilon, \lambda_\mu) > 0$, while an oblate ellipsoid results from $f_d(\lambda_\sigma, \lambda_\varepsilon, \lambda_\mu) < 0$.

A grid independence test is performed using three different grid systems. The grid resolutions R/Δ are chosen to be 12, 16, and 20. As shown in Fig. 3, the simulation results are almost the same for three different grid systems. Thus, the grid resolution is chosen to be $R/\Delta = 16$ for the following simulations. The dimensionless flow time T is defined as

$$T = \frac{t}{\mu_o/\varepsilon_0\varepsilon_o E_0^2}. \qquad (28)$$

B. Results and discussion

Figure 4 shows the deformation rates of a leaky dielectric droplet in the electric field. As shown in Figs. 4(a) and 4(b), the deformation rate increases almost linearly with the increase of electric capillary number Ca_E for small droplet
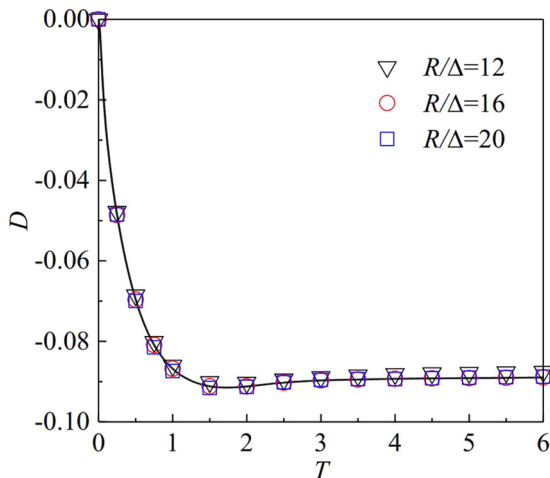

FIG. 3. Evolution of the droplet deformation rate with time for three different grid systems ($\lambda_\sigma = 0.5$, $\lambda_\varepsilon = 2$, $\lambda_\mu = 1$, $Ca_E = 0.2$).
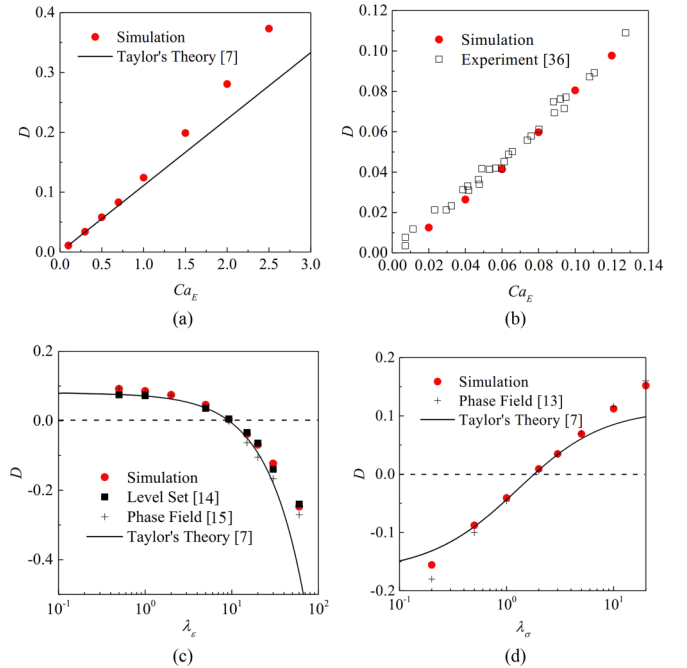

FIG. 4. Droplet deformation rates: (a) $\lambda_\sigma = 2.5$, $\lambda_\varepsilon = 2$, $\lambda_\mu = 1$; (b) $\lambda_\sigma = 100$, $\lambda_\varepsilon = 17.54$, $\lambda_\mu = 0.00071$; (c) $\lambda_\sigma = 5$, $\lambda_\mu = 16$, $Ca_E = 0.2$; and (d) $\lambda_\varepsilon = 2$, $\lambda_\mu = 1$, $Ca_E = 0.2$.

deformation ($D \leqslant 0.1$). As the electric capillary number Ca_E continues to increase ($D > 0.1$), the droplet deformation increases dramatically. It should be noted that the electric conductivity ratio λ_σ is greater than 10 000 in the experiment [36], which has been viewed as a challenge for present two-phase flow models. Fortunately, the system behaves just as if an uncharged conducting drop in an insulating fluid when the electric conductivity ratio λ_σ is greater than 100. The increase of λ_σ hardly affects droplet behavior [37]. Therefore, the conductivity ratio λ_σ is set to be 100 in Fig. 4(b). Figure 4(c) shows that the terminal droplet shape in the electric field transforms from a prolate ellipsoid to an oblate ellipsoid as the permittivity ratio λ_ε increases. When the deformation rate is greater than 0, the permittivity ratio λ_ε shows only a limited effect on droplet deformation. However, when the deformation rate is smaller than 0, the droplet deformation increases rapidly with the increase of permittivity ratio λ_ε. All the above results fit well with Lin's numerical results [14,15]. In Fig. 4(d), the electric conductivity ratio λ_σ is changed while other parameters are kept constant. Simulation results are in good agreement with Yang's numerical predictions [13]. The terminal droplet shape transforms from an oblate ellipsoid to a prolate ellipsoid while increasing the electric conductivity ratio λ_σ from 0.2 to 20. The relationship between deformation rate and the common logarithm of electric conductivity ratio is approximatively linear [12,13].

Simulation results are also compared with Taylor's theoretical predictions [7]. It is obvious that the simulation and theoretical predictions agree only reasonably well for small droplet deformation ($|D| \leqslant 0.05$). There are great differences between the simulation results and theoretical predictions for large droplet deformation, since the theoretical model is based on the small deformation hypothesis [12,15].
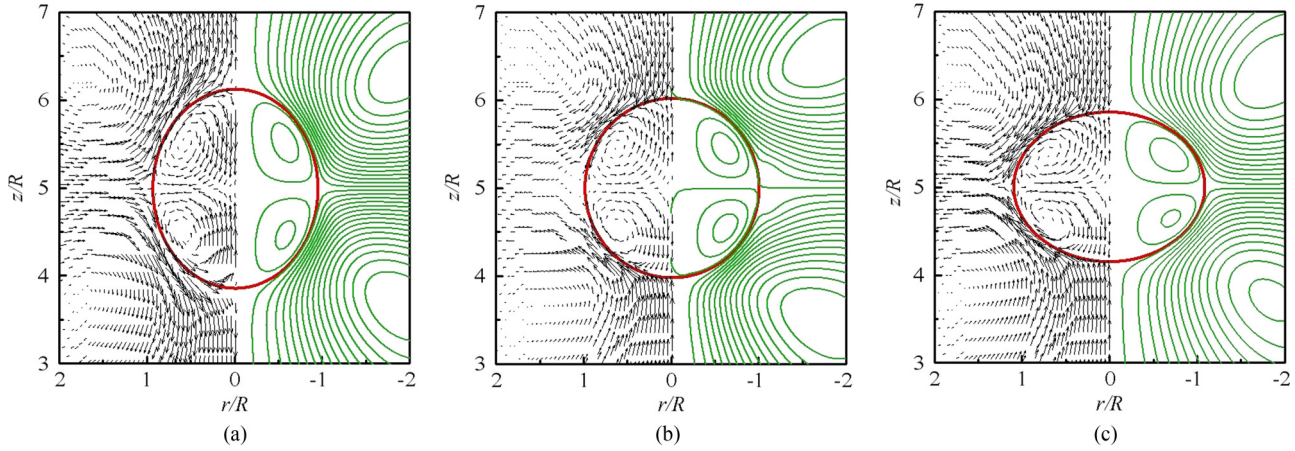
FIG. 5. Velocity vectors (left) and stream functions (right) around the droplet at $y = 5R$: (a) $\lambda_\sigma = 5$, $\lambda_\varepsilon = 0.5$, $\lambda_\mu = 16$, $Ca_E = 0.2$, $D = 0.092$; (b) $\lambda_\sigma = 5$, $\lambda_\varepsilon = 8$, $\lambda_\mu = 16$, $Ca_E = 0.2$, $D = 0.014$; and (c) $\lambda_\sigma = 5$, $\lambda_\varepsilon = 30$, $\lambda_\mu = 16$, $Ca_E = 0.2$, $D = -0.123$.

Figure 5 shows the velocity vectors (left) and stream functions (right) around the droplet at $y = 5R$ for different parameters. Four identical vortices are generated inside and outside of the droplet, respectively. When $\lambda_\varepsilon = 0.5$ [Fig. 5(a)], the droplet takes the form of a prolate ellipsoid and fluid flows from the droplet equator to the axis poles along the droplet interface. When $\lambda_\varepsilon = 30$ [Fig. 5(c)], the droplet takes the form of an oblate ellipsoid and the fluid motion direction is totally reversed. Interestingly, the fluid motion direction of a prolate droplet with small deformation [Fig. 5(b)] is also reversed to the droplet with large deformation [Fig. 5(a)]. All of these are in good agreement with previous results [12,14,15].

The generated flow field inside the droplet suggests that an isolated droplet is an efficient microreactor to induce the liquid mixture. The effectiveness is greatly influenced by the circulatory flow velocity. Figure 6(a) shows the velocity magnitude distributions around the droplet when $\lambda_\sigma = 0.2$, $\lambda_\varepsilon = 2$, $\lambda_\mu = 1$, $Ca_E = 0.2$ at $y = 5R$. The maximum velocity lies near the droplet interface. Accordingly, Figs. 6(b)–6(d) shows the dimensionless maximum velocity magnitudes near the droplet interface for different parameters. The dimensionless maximum velocity magnitude U is obtained by

$$U = \frac{|\boldsymbol{u}|_{\max}}{\sqrt{\gamma/\rho_o R}}. \tag{29}$$

Figure 6(b) shows that the circulatory flow velocity increases almost linearly with the increase of electric capillary number Ca_E. According to Figs. 6(c) and 6(d), the circulatory flow direction and magnitude are also influenced by the relative magnitude of electric conductivity ratio and permittivity ratio. The velocity magnitude is almost zero when $\lambda_\varepsilon = \lambda_\sigma$. The maximum velocity magnitude experiences a slow increase with the decrease of λ_ε or the increase of λ_σ when $\lambda_\sigma > \lambda_\varepsilon$. The maximum velocity magnitude experiences a significant increase with the increase of λ_ε or the decrease of λ_σ when $\lambda_\sigma < \lambda_\varepsilon$. The circulatory flow directions around the droplet are also shown in Figs. 6(c) and 6(d) and are consistent with Fig. 5. To sum up, the fluid flow velocity has a drastic variation for $\lambda_\sigma/\lambda_\varepsilon < 1$. However, the variation is not so drastic for $\lambda_\sigma/\lambda_\varepsilon > 1$. A droplet with $\lambda_\sigma/\lambda_\varepsilon < 1$ has greater potential to be used as a microreactor.

After the droplet deforms into an ellipsoid, the electric field intensity in the droplet $\boldsymbol{E}_i$ is uniform and has the same direction as the external electric field $\boldsymbol{E}_0$ [38]:

$$\boldsymbol{E}_i = \frac{\sigma_o}{(1-n)\sigma_o + n\sigma_i}\boldsymbol{E}_0,$$

$$n = \frac{1-e^2}{2e^3}\left(\ln\frac{1+e}{1-e} - 2e\right),$$

$$e = \sqrt{1 - B^2/L^2}. \tag{30}$$

When the droplet and external fluid are exposed to the electric field, the free charges accumulate on the interface. The

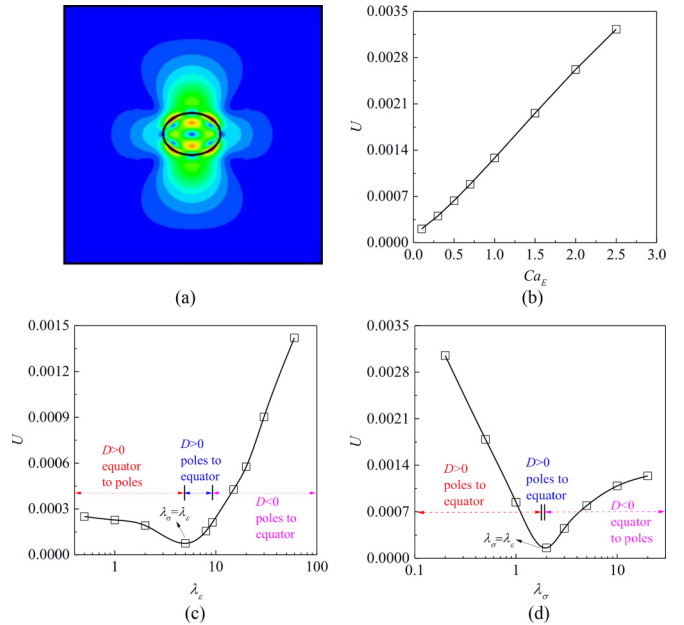FIG. 6. (a) Velocity magnitude distributions around the droplet at $y = 5R$ when $\lambda_\sigma = 0.2$, $\lambda_\varepsilon = 2$, $\lambda_\mu = 1$, $Ca_E = 0.2$. The red color corresponds to high velocity while the blue color corresponds to low velocity. (b)–(d) The dimensionless maximum velocity magnitude near the droplet interface. (b) $\lambda_\sigma = 2.5$, $\lambda_\varepsilon = 2$, $\lambda_\mu = 1$; (c) $\lambda_\sigma = 5$, $\lambda_\mu = 16$, $Ca_E = 0.2$; and (d) $\lambda_\varepsilon = 2$, $\lambda_\mu = 1$, $Ca_E = 0.2$.
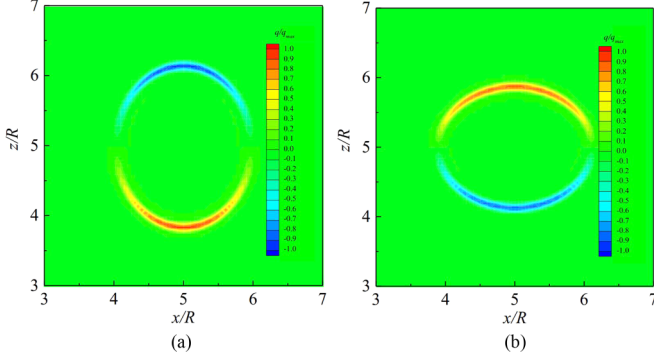
FIG. 7. Distribution of volume density of local free charges q at $y = 5R$: (a) $\lambda_\sigma = 5$, $\lambda_\varepsilon = 0.5$, $\lambda_\mu = 1$, $Ca_E = 0.2$; and (b) $\lambda_\sigma = 5$, $\lambda_\varepsilon = 30$, $\lambda_\mu = 1$, $Ca_E = 0.2$.

surface charge density q_s at the droplet interface is obtained by

$$q_s = \varepsilon_0 \varepsilon_i E_{in} - \varepsilon_0 \varepsilon_o \frac{\sigma_i E_{in}}{\sigma_o} = \varepsilon_0 \varepsilon_i \left(1 - \frac{\lambda_\sigma}{\lambda_\varepsilon}\right) E_{in}, \quad (31)$$

where E_{in} is the component of electric field intensity $\boldsymbol{E}_i$ normal to the interface in the droplet. $\boldsymbol{E}_{in}$ is always positive on the top interface while it is always negative on the bottom interface. The surface charge density $\boldsymbol{q}_s$ is fully decided by $\lambda_\sigma/\lambda_\varepsilon$. The negative charges accumulate on the top interface while the positive charges accumulate on the bottom interface when $\lambda_\sigma/\lambda_\varepsilon > 1$. The positive charges accumulate on the top interface while the negative charges accumulate on the bottom interface when $\lambda_\sigma/\lambda_\varepsilon < 1$. The distributions of

volume density of local free charges q when $\lambda_\sigma = 5$, $\lambda_\varepsilon = 0.5$, $\lambda_\mu = 1$, $Ca_E = 0.2$ and $\lambda_\sigma = 5$, $\lambda_\varepsilon = 30$, $\lambda_\mu = 1$, $Ca_E = 0.2$ are shown in Fig. 7. They are consistent with Eq. (31).

Interestingly, although the distribution of volume density of local free charges q is fully decided by $\lambda_\sigma/\lambda_\varepsilon$, the direction of electric force cannot be simply decided by the nature of free charges between the electrode and the droplet interface, which is in contrast with the results of Nath *et al.* [39]. For the droplet without deformation, the electric stress components along the normal direction $\|\tau_{rr}^e\|$ and tangential direction $\|\tau_{r\theta}^e\|$ at the interface are given by [10]

$$\|\tau_{rr}^e\| = \frac{9\varepsilon_0 \varepsilon_o E_0^2}{4(\lambda_\sigma + 2)^2}\left[(\lambda_\sigma^2 - 2\lambda_\varepsilon + 1)\cos^2\theta + \lambda_\varepsilon - 1\right], \quad (32)$$

$$\|\tau_{r\theta}^e\| = \frac{9\varepsilon_0 \varepsilon_o E_0^2}{4(\lambda_\sigma + 2)^2}(\lambda_\varepsilon - \lambda_\sigma)\sin 2\theta, \quad (33)$$

where θ is the polar angle measured from the electric field direction in the clockwise direction. The electric stress along the tangential direction is zero at the droplet axis poles and equator ($\theta = 0°$ and $90°$). As a result, the electric stress at the droplet axis poles ($\theta = 0°$) point toward the outside of the droplet when $\lambda_\sigma^2 > \lambda_\varepsilon$ while it points toward the inside of droplet when $\lambda_\sigma^2 < \lambda_\varepsilon$. The electric stress at the droplet equator ($\theta = 90°$) points toward the outside of the droplet when $\lambda_\varepsilon > 1$ while it points toward the inside of the droplet when $\lambda_\varepsilon < 1$. The electric stress along the tangential direction is influenced by the values of $\lambda_\sigma/\lambda_\varepsilon$ and $\sin 2\theta$ at the same time.
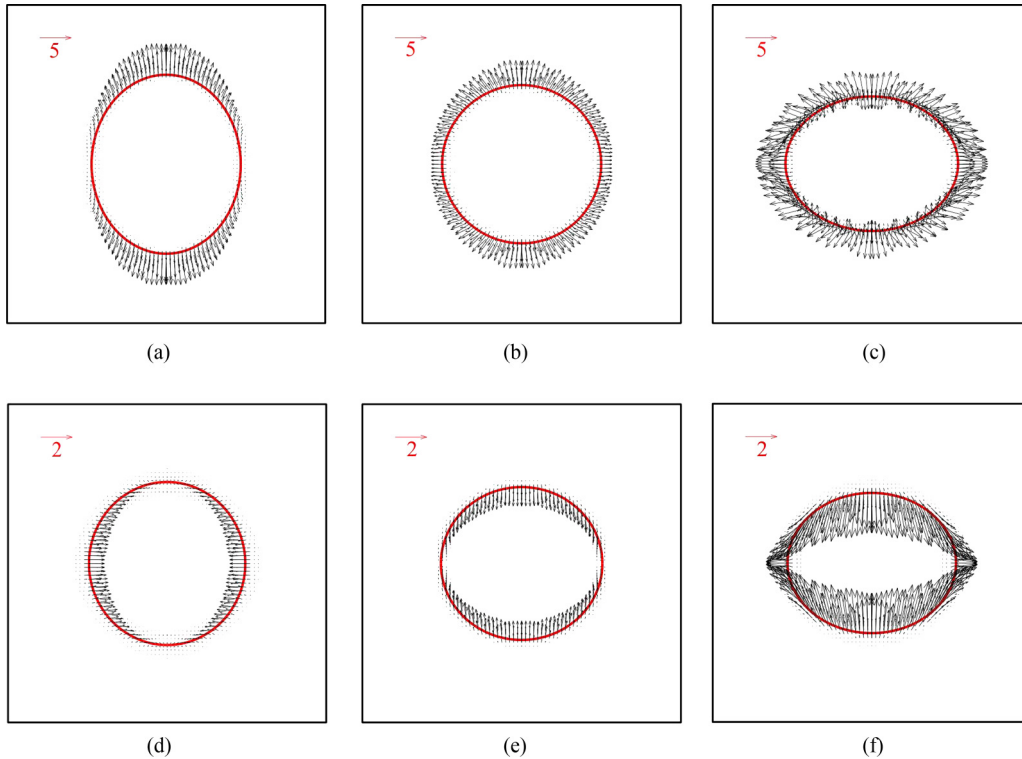

FIG. 8. Electric force distribution around the droplet interface at $y = 5R$: (a) $\lambda_\sigma = 5$, $\lambda_\varepsilon = 0.5$, $\lambda_\mu = 1$, $Ca_E = 0.2$. $D > 0$; (b) $\lambda_\sigma = 5$, $\lambda_\varepsilon = 10$, $\lambda_\mu = 1$, $Ca_E = 0.2$, $D \approx 0$; (c) $\lambda_\sigma = 5$, $\lambda_\varepsilon = 30$, $\lambda_\mu = 1$, $Ca_E = 0.2$, $D < 0$; (d) $\lambda_\sigma = 0.5$, $\lambda_\varepsilon = 0.2$, $\lambda_\mu = 1$, $Ca_E = 0.2$, $D > 0$; (e) $\lambda_\sigma = 0.5$, $\lambda_\varepsilon = 1$, $\lambda_\mu = 1$, $Ca_E = 0.2$, $D < 0$; and (f) $\lambda_\sigma = 0.5$, $\lambda_\varepsilon = 2$, $\lambda_\mu = 1$, $Ca_E = 0.2$, $D < 0$.
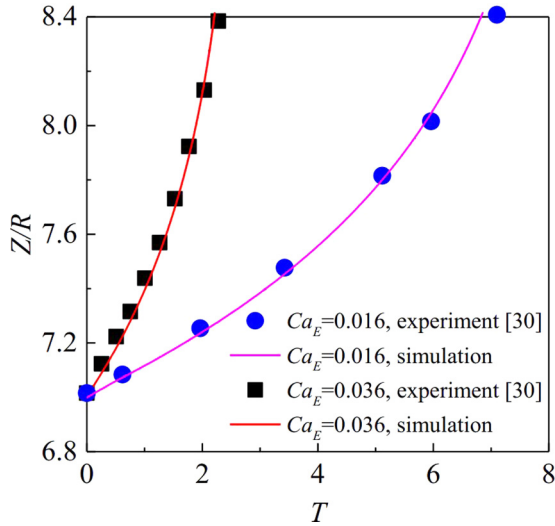
FIG. 9. Transient development of droplet position along z direction when $\lambda_\sigma = 100$, $\lambda_\varepsilon = 17.02$, $\lambda_\rho = 1.04$, and $\lambda_\mu = 0.0013$.

Figure 8 shows the electric force $\boldsymbol{F}_e$ distributions around the droplet interface at $y = 5R$ for different parameters. The electric force $\boldsymbol{F}_e$ is nondimensionalized by

$$|\boldsymbol{F}_e^n| = \frac{|\boldsymbol{F}_e|}{\gamma/R^2}. \tag{34}$$

The electric force could act toward the outside or inside of the droplet and produce different droplet deformations. The direction of electric force has a good agreement with above analyses. In Figs. 8(a)–8(c), the electric force acts toward the outside of the droplet. When $\lambda_\sigma = 5$ and $\lambda_\varepsilon = 0.5$ [Fig. 8(a)], the electric force at the droplet axis poles is stronger than that at the equator and produces a prolate ellipsoid droplet. With the increase of permittivity ratio λ_ε, the electric force at the droplet equators increases [Fig. 8(b)]. When the permittivity ratio λ_ε is large enough [Fig. 8(c)], the electric force at the
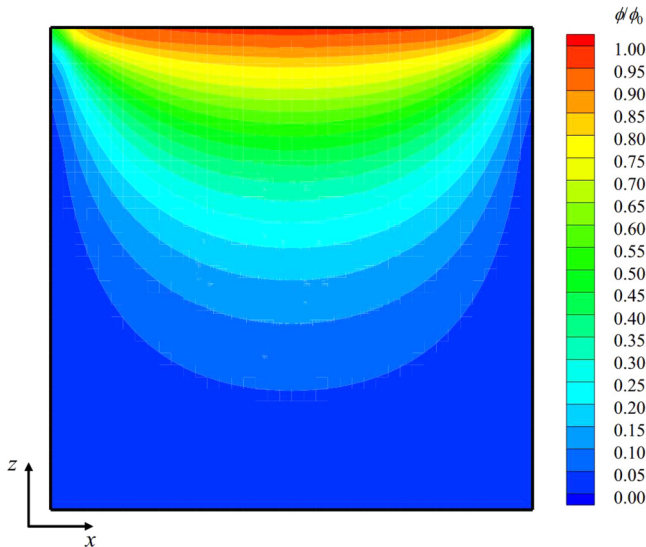

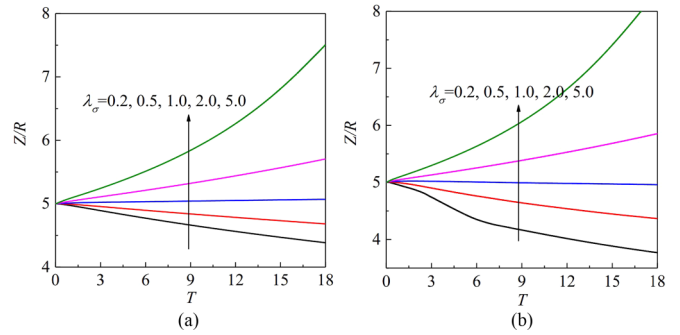FIG. 10. Electric potential distribution at $y = 5R$ when the droplet does not exist.

FIG. 11. Transient development of droplet position along z direction: (a) $\lambda_\varepsilon = 2$, $\lambda_\mu = 1$, $\mathrm{Ca}_E = 0.2$ and (b) $\lambda_\varepsilon = 10$, $\lambda_\mu = 1$, $\mathrm{Ca}_E = 0.2$.

droplet axis poles is smaller than that at the equator and produces an oblate ellipsoid droplet. In Figs. 8(d)–8(f), the electric force acts toward the inside of the droplet. When $\lambda_\sigma = 0.5$ and $\lambda_\varepsilon = 0.2$ [Fig. 8(d)], the electric force at the droplet equator is stronger than that at the axis poles and produces a prolate ellipsoid droplet. With the increase of permittivity ratio λ_ε, the electric force at the droplet axis poles increases while the force at the equator decreases [Fig. 8(e)]. When the permittivity ratio λ_ε is large enough [Fig. 8(f)], the electric force at the equator even acts toward the outside of the droplet. Both of the electric forces at the equator and axis poles produce an oblate ellipsoid droplet.

IV. DROPLET IN THE NONUNIFORM ELECTRIC FIELD

The electric force around the droplet is no longer symmetric in the nonuniform electric field. Besides employing the $\lambda_\sigma = 100$, $\lambda_\varepsilon = 17.02$, $\lambda_\rho = 1.04$, $\lambda_\mu = 0.0013$, a theoretical simulation model, which possessed a similar architecture configuration as that of the experiment, is constructed [30]. Although the electric conductivity ratio λ_σ is greater than 1 000 000 in the experiment, it is set to be 100 during the simulation, which hardly affects droplet behaviors [37]. The
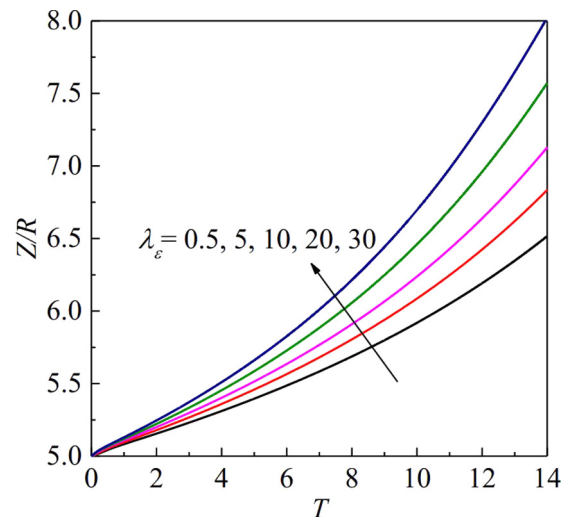

FIG. 12. Transient development of droplet position along z direction when $\lambda_\sigma = 5$, $\lambda_\mu = 1$, $\mathrm{Ca}_E = 0.2$.
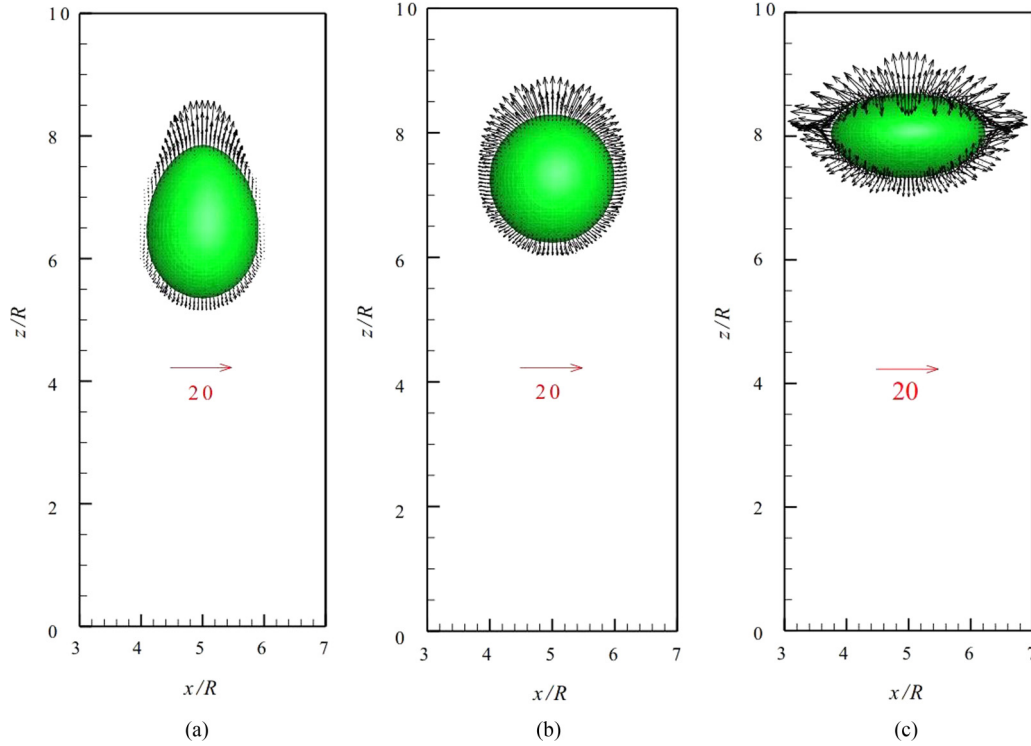
FIG. 13. Droplet deformation and electric force distribution at $y = 5R$ in the moment of $T = 14$: (a) $\lambda_\sigma = 5$, $\lambda_\varepsilon = 0.5$, $\lambda_\mu = 1$, $Ca_E = 0.2$; (b) $\lambda_\sigma = 5$, $\lambda_\varepsilon = 10$, $\lambda_\mu = 1$, $Ca_E = 0.2$; and (c) $\lambda_\sigma = 5$, $\lambda_\varepsilon = 30$, $\lambda_\mu = 1$, $Ca_E = 0.2$.

droplet would migrate toward the electrode in the pin-plate electrode system for high electric field intensity [30]. The transient development of the droplet position along z direction is shown in Fig. 9. The dimensionless flow time T is defined as Eq. (28). The droplet position Z is evaluated by

$$Z = \frac{\int z\alpha_i dxdydz}{\int \alpha_i dxdydz}. \qquad (35)$$

The simulation results are in good agreement with the experiments [30].

For ease of comparison, the droplet behaviors in the nonuniform electric field are simulated using the same geometry, as shown in Fig. 1. The boundary conditions for the electric potential are adjusted to generate a nonuniform

electric field with great inhomogeneity:

$$
\begin{aligned}
z = 10R, &\quad \text{no-slip wall}, &\quad \phi = \phi_0 \\
z = 0, &\quad \text{no-slip wall}, &\quad \phi = 0 \\
x = 10R, &\quad \text{no-slip wall}, &\quad \phi = 0 \\
x = 0, &\quad \text{no-slip wall}, &\quad \phi = 0 \\
y = 10R, &\quad \text{no-slip wall}, &\quad \phi = 0 \\
y = 0, &\quad \text{no-slip wall}, &\quad \phi = 0.
\end{aligned}
\qquad (36)
$$

The electric potential distribution at $y = 5R$ when the droplet does not exist is shown in Fig. 10. The electric potential profiles are intensive near the top plates while the electric potential profiles are sparse near the bottom plates. Because the electric field intensity is the negative gradient of
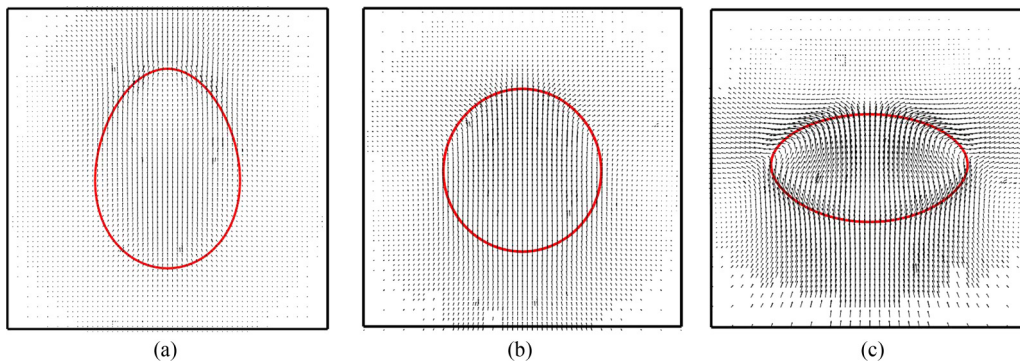

FIG. 14. Droplet velocity fields at $y = 5R$ in the moment of $T = 14$: (a) $\lambda_\sigma = 5$, $\lambda_\varepsilon = 0.5$, $\lambda_\mu = 1$, $Ca_E = 0.2$; (b) $\lambda_\sigma = 5$, $\lambda_\varepsilon = 10$, $\lambda_\mu = 1$, $Ca_E = 0.2$; and (c) $\lambda_\sigma = 5$, $\lambda_\varepsilon = 30$, $\lambda_\mu = 1$, $Ca_E = 0.2$.

electric potential, it is larger at the position with more intensive electric potential profiles. As a result, the electric field intensity increases along the positive z direction. The droplet experiences deformation and dielectrophoretic migration at the same time.

The effects of a symmetric nonuniform electric field on droplet behaviors are investigated by initially setting a spherical droplet with a radius R in the center of a cubic cavity. The electric force around the droplet is only asymmetric along the z direction. As a result, the droplet experiences deformation and dielectrophoretic migration only along the z direction. Figure 11 shows the transient development of droplet position along z direction for different electric conductivity ratios λ_σ when $\lambda_\varepsilon = 2$, $\lambda_\mu = 1$, $Ca_E = 0.2$ [Fig. 11(a)] and $\lambda_\varepsilon = 10$, $\lambda_\mu = 1$, $Ca_E = 0.2$ [Fig. 11(b)]. The electric conductive ratio λ_σ increases along the arrow direction. The droplet migrates along the positive z direction when $\lambda_\sigma > 1$, while the droplet migrates along the negative z direction when $\lambda_\sigma < 1$. The droplet migration velocity increases with the increase of electric conductivity ratio λ_σ when $\lambda_\sigma > 1$, while the velocity increases with the decrease of electric conductive ratio λ_σ when $\lambda_\sigma < 1$. In other words, a greater difference between the electric conductivities of droplet and external fluid always leads to a greater migration velocity.

Figure 12 shows the transient development of droplet position along the z direction for different permittivity ratios λ_ε when $\lambda_\sigma = 5$, $\lambda_\mu = 1$, $Ca_E = 0.2$. The droplet height has an evident increase as the permittivity ratios λ_ε increases, as shown by the arrow. Accordingly, the droplet migration velocity increases. The droplet shapes and corresponding electric force distributions at $y = 5R$ in the moment of $T = 14$ are shown in Fig. 13. Corresponding to Figs. 8(a)–8(c), the electric force also acts toward the outside of the droplet in the nonuniform electric field. Because the electric field intensity increases along the positive z direction, the electric force at the top half of the droplet is greater than that at the bottom half of the droplet and an upward force is produced. The droplet is stretched along the electric field direction and produces a sharp tip when $\lambda_\varepsilon = 0.5$. The increase of λ_ε inhibits the droplet from being stretched, and the droplet even takes the form of an oblate shape when $\lambda_\varepsilon = 30$. As a result, the action area of electric force becomes larger with the increase of permittivity ratio λ_ε and produces a larger upward force. In addition, as the droplet goes up to where the electric field is stronger, the electric force increases and leads to a greater velocity. Namely, the slope of the curve increases with time in Fig. 12. Figure 14 shows the droplet velocity fields at $y = 5R$ in the moment of $T = 14$. A larger velocity always corresponds to a larger permittivity ratio λ_ε, which is consistent with Fig. 12. Additionally, because of the migration of the droplet, the vortices which existed in the uniform electric field disappear. The hydrodynamic force has only a small influence on droplet migration compared with the electric force.

Comparing with Fig. 13(b), when the electric conductivity ratio λ_σ decreases from 5 to 2, the electric force acts toward the inside of the droplet because $\lambda_\sigma^2 < \lambda_\varepsilon$, as shown in Fig. 15. However, the action area of downward electric force is much smaller compared with the upward electric force. A detailed calculation shows that an upward electric force is finally produced. Besides, because the circulatory flow
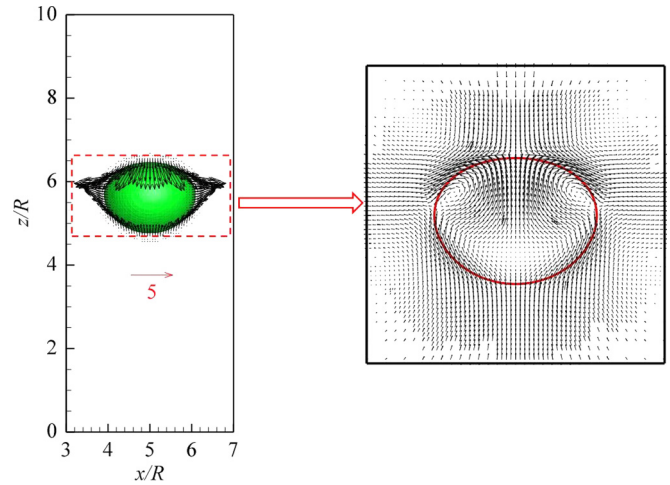

FIG. 15. Droplet deformation, electric force distribution (left), and the corresponding velocity fields (right) at $y = 5R$ in the moment of $T = 14$ when $\lambda_\sigma = 2$, $\lambda_\varepsilon = 10$, $\lambda_\mu = 1$, $Ca_E = 0.2$.

velocity has a significant increase with the decrease of λ_σ (Fig. 6). The vortices do not disappear in the nonuniform electric field. An upward hydrodynamic force is also produced [15]. The droplet migrates along the positive z direction, as shown in Fig. 11(b).

Figure 16 shows the transient development of droplet position along z direction for different permittivity ratios λ_ε when $\lambda_\sigma = 0.5$, $\lambda_\mu = 1$, $Ca_E = 0.2$. Corresponding to Figs. 8(d)–8(f), the electric force also acts toward the inside of the droplet in the nonuniform electric field. Because the electric field intensity increases along the positive z direction, the electric force at the top half of the droplet is greater than that at the bottom half of the droplet and a downward force is produced. The droplet height has an evident decrease when the permittivity ratios λ_ε increase from 2 to 30, as shown by the arrow. Accordingly, the droplet migration velocity increases. The droplet shapes and corresponding electric force
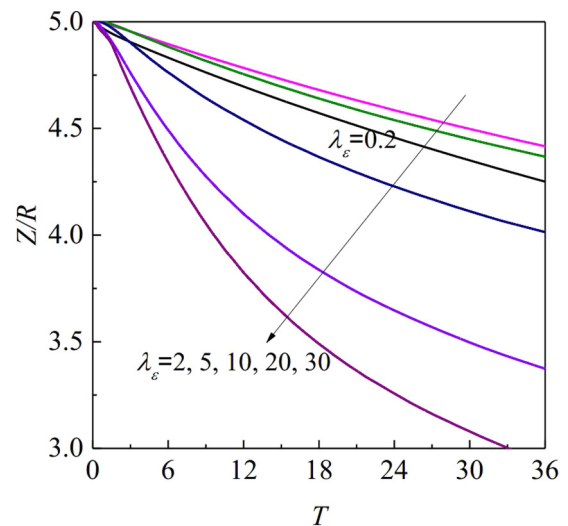

FIG. 16. Transient development of droplet position along z direction when $\lambda_\sigma = 0.5$, $\lambda_\mu = 1$, $Ca_E = 0.2$.
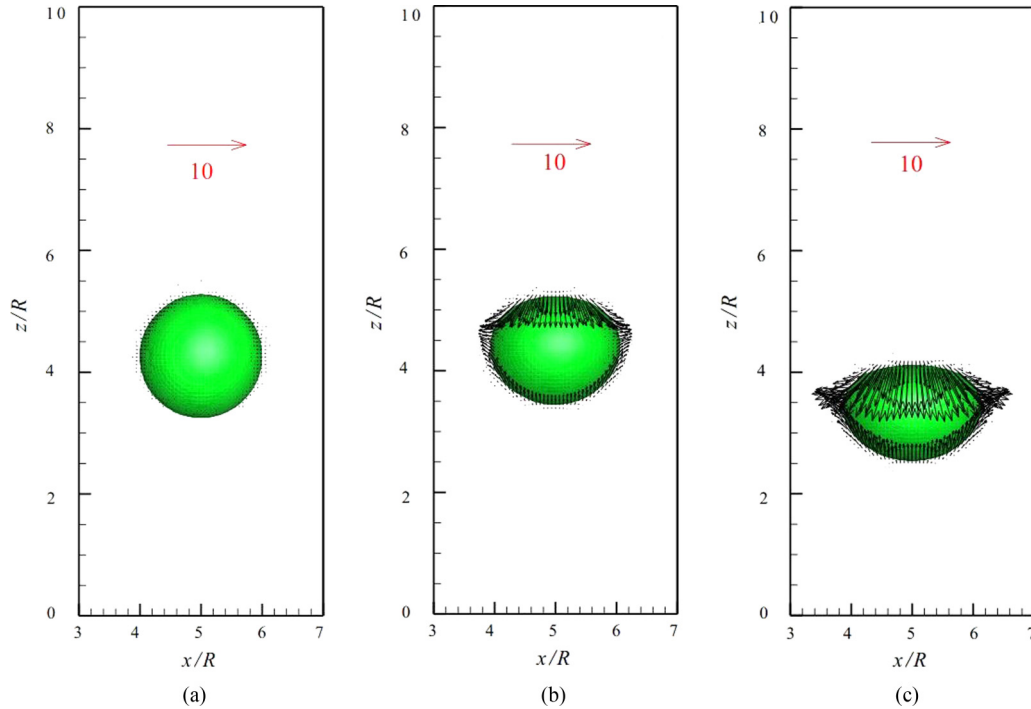
FIG. 17. Droplet deformation and electric force distribution at $y = 5R$ in the moment of $T = 14$: (a) $\lambda_\sigma = 0.5$, $\lambda_\varepsilon = 0.2$, $\lambda_\mu = 1$, $\text{Ca}_E = 0.2$; (b) $\lambda_\sigma = 0.5$, $\lambda_\varepsilon = 5$, $\lambda_\mu = 1$, $\text{Ca}_E = 0.2$; and (c) $\lambda_\sigma = 0.5$, $\lambda_\varepsilon = 20$, $\lambda_\mu = 1$, $\text{Ca}_E = 0.2$.

distributions at $y = 5R$ in the moment of $T = 14$ are shown in Fig. 17. The droplet is compressed along the electric field direction with the increase of permittivity ratio λ_ε. In addition, the downward electric force also has a great increase and increases the droplet migration velocity. What is unusual is that when λ_ε increases from 0.2 to 2, the droplet migration velocity has a slight decrease. The migration velocity when $\lambda_\varepsilon = 0.2$ is even greater than $\lambda_\varepsilon = 5$. Figure 18 shows the droplet velocity fields at $y = 5R$ in the moment of $T = 14$. There exists no vortices when $\lambda_\varepsilon = 0.2$. However, with the increase of permittivity ratio λ_ε the vortices begin to appear. Because the circulatory flow velocity around the top half of the droplet is greater than that around the bottom half of the droplet, an upward hydrodynamic force hinders the migration of the droplet along the negative z direction [15]. Because the hydrodynamic force is smaller than the electric force, the

droplet migration velocity has only a minor decrease. When the permittivity ratio is large enough, the electric force begins to dominate droplet migration and the droplet velocity begins to increase dramatically. In addition, as the droplet moves down to where the electric field is weaker, the electric force decreases, leading to a smaller velocity. Namely, the slope of the curve decreases with time in Fig. 16. Furthermore, because the droplet migrates toward a stronger electric field for $\lambda_\sigma = 5$ while the droplet migrates toward a weaker electric field for $\lambda_\sigma = 0.5$, the droplet migration velocity is much faster when $\lambda_\sigma = 5$ than that when $\lambda_\sigma = 0.5$, as shown in Figs. 12 and 16.

Comparing with Fig. 17(a), when the electric conductivity ratios λ_σ increase from 0.5 to 0.8, the direction of electric force is not uniform any longer, as shown in Fig. 19. A detailed calculation shows that a downward electric force is
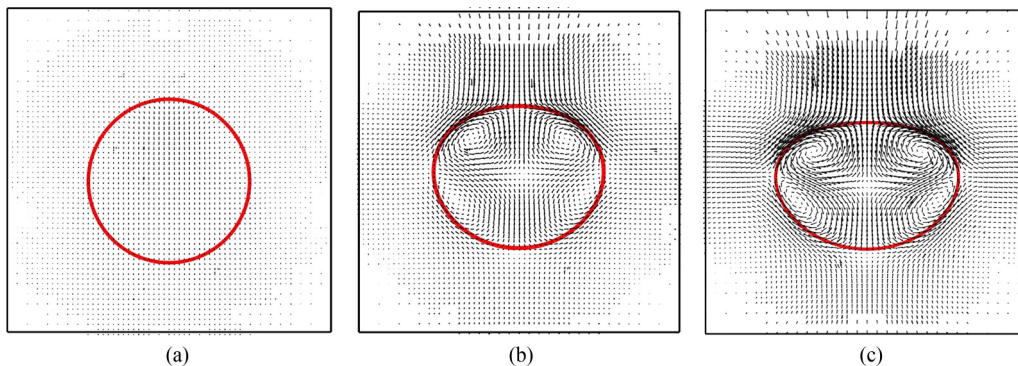

FIG. 18. Droplet velocity fields at $y = 5R$ in the moment of $T = 14$: (a) $\lambda_\sigma = 0.5$, $\lambda_\varepsilon = 0.2$, $\text{Ca}_E = 0.2$; (b) $\lambda_\sigma = 0.5$, $\lambda_\varepsilon = 5$, $\text{Ca}_E = 0.2$; and (c) $\lambda_\sigma = 0.5$, $\lambda_\varepsilon = 20$, $\text{Ca}_E = 0.2$.
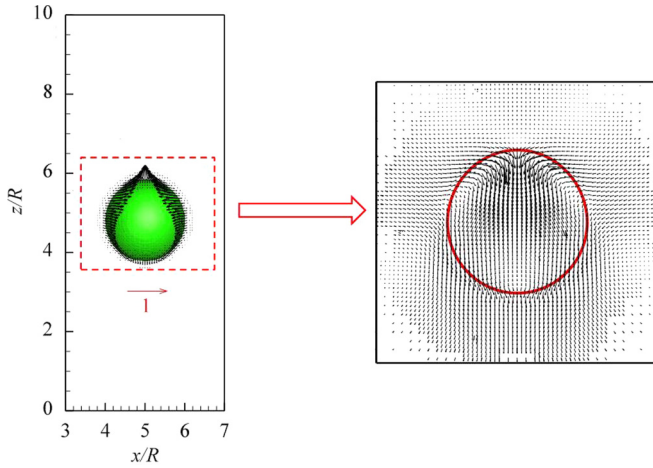
FIG. 19. Droplet deformation, electric force distribution (left), and the corresponding velocity fields (right) at $y = 5R$ in the moment of $T = 14$ when $\lambda_\sigma = 0.8$, $\lambda_\varepsilon = 0.2$, $\lambda_\mu = 1$, and $\mathrm{Ca}_E = 0.2$.

also produced. No apparent vortices appear in the nonuniform electric field. The droplet migrates along the negative z direction. Because the magnitude of electric force is much smaller compared with Fig. 17, the migration velocity is very small.

Figure 20 shows the transient development of droplet position along the z direction for different electric capillary numbers Ca_E when $\lambda_\sigma = 5$, $\lambda_\varepsilon = 2$, $\lambda_\mu = 1$. The droplet velocity has a dramatic increase when the electric capillary number Ca_E increases from 0.1 to 0.4 because of the increase of electric force, as shown by the arrow.

To have a better understanding of the droplet behaviors in a more general sense, the effects of an asymmetric nonuniform electric field on droplet behavior are also investigated by setting a spherical droplet with a radius R in the position $(7R, 5R, 5R)$ in the beginning. The surrounding electric field is asymmetric along x and z directions at the same time. Figure 21 shows the evolution of droplet positions and corresponding electric force distributions at $y = 5R$ when $\lambda_\sigma = 5$,
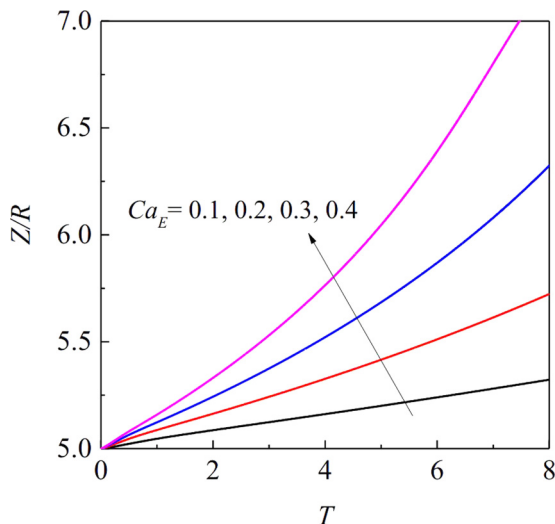

FIG. 20. Transient development of droplet position along z direction when $\lambda_\sigma = 5$, $\lambda_\varepsilon = 2$, $\lambda_\mu = 1$.

$\lambda_\varepsilon = 2$, $\lambda_\mu = 1$, $\mathrm{Ca}_E = 0.2$. The droplet is stretched along the electric field direction and produces a sharp tip as shown in Fig. 13. However, because the electric force is no longer symmetric along the x direction, the electric force has a certain amount of declination along the negative x direction, as well as the sharp tip of the droplet. The droplet also has a slight migration along the negative x direction. Figure 22 shows the evolution of droplet positions and corresponding electric force distributions at $y = 5R$ when $\lambda_\sigma = 0.5$, $\lambda_\varepsilon = 2$, $\lambda_\mu = 1$, and $\mathrm{Ca}_E = 0.2$. The droplet is compressed along the electric field direction as shown in Fig. 17. Because the direction of electric force is reversed in Fig. 20, the electric force has a certain amount of declination along the positive x direction. The droplet also has a slight migration along the positive x direction. Overall, the droplet tends to experience deformation and dielectrophoretic migration along the normal direction of electric potential profiles.

V. CONCLUSIONS

In this work, a VOF+LS+SPP method, which is applied to simulate the dynamic behaviors of perfect dielectric droplets, is extended to the simulation of three-dimensional leaky dielectric droplets in the electric field. The dynamically adaptive grid technique, which is effective to improve simulation accuracy and save computer resources at the same time, is applied to refine the region around the droplet interface. Salient findings and conclusions are summarized as follows:

(1) Simulation results about the deformation and fluid motions of a single droplet in the uniform electric field are in good agreement with previous theoretical and numerical predictions, proving the feasibility of the three-dimensional VOF+LS+SPP method. Four identical vortices are generated inside the droplet under the action of uniform electric field. The variation of circulatory flow velocity is drastic for $\lambda_\sigma/\lambda_\varepsilon < 1$ but gentle for $\lambda_\sigma/\lambda_\varepsilon > 1$. A droplet with $\lambda_\sigma/\lambda_\varepsilon < 1$ is more efficient as a microreactor. Although the distribution of free charges around the droplet is fully decided by $\lambda_\sigma/\lambda_\varepsilon$, the electric force distribution cannot simply be decided by the nature of free charges between the electrode and the droplet interface. The electric force could act toward the outside or inside of a droplet and produce different droplet deformations.

(2) A droplet in a nonuniform electric field experiences deformation and dielectrophoretic migration at the same time. Under the combined actions of electric and hydrodynamic forces, the droplet migrates toward a stronger electric field when $\lambda_\sigma > 1$. In most cases, the electric force acts toward the outside of the droplet. The electric force at the top half of the droplet is greater than that at the bottom half of the droplet. An upward electric force is produced. When the electric conductivity ratio is much smaller than the permittivity ratio, the electric force acts toward the inside of the droplet. Interestingly, the electric force at the top half of the droplet is smaller than that at the bottom half of the droplet, and an upward electric force is also produced. As a result, the droplet migrates toward the stronger electric field in these two circumstances. With the increase of permittivity ratio λ_ε, the droplet is compressed along the electric field. The electric force increases and produces greater migration
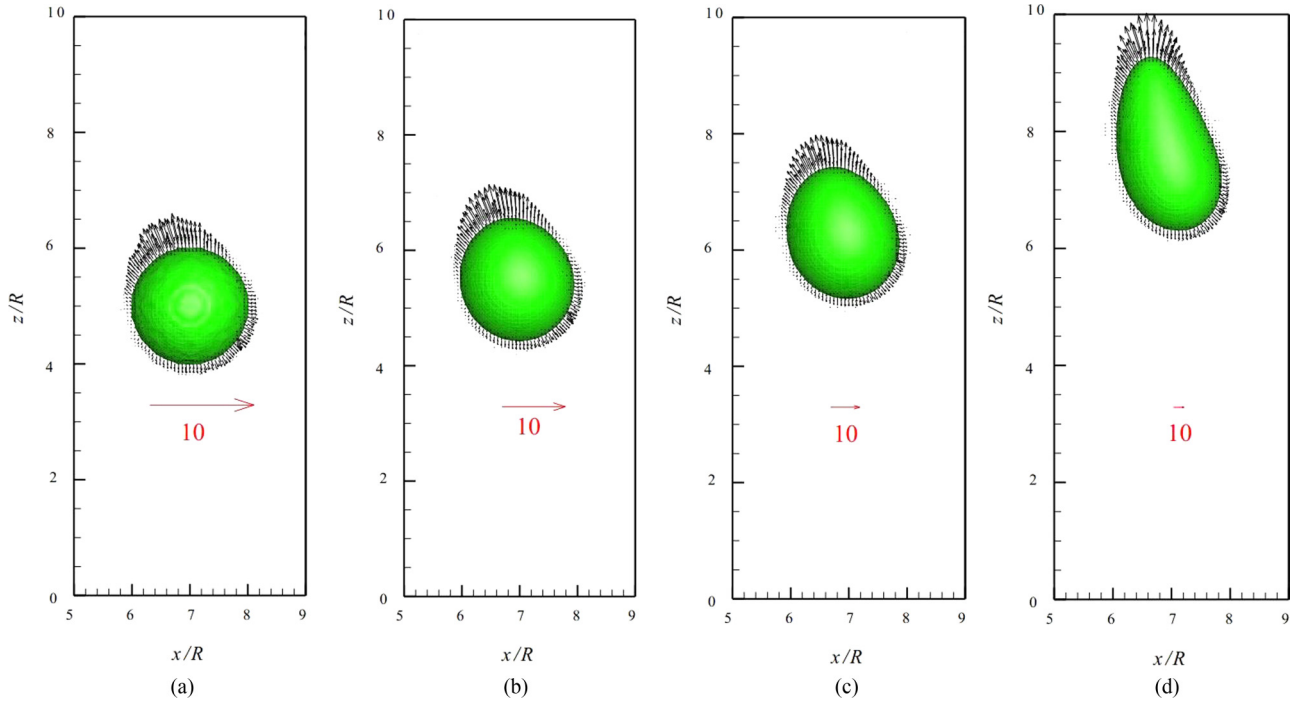
FIG. 21. Evolution of droplet positions and corresponding electric force distributions at $y = 5R$ when $\lambda_\sigma = 5$, $\lambda_\varepsilon = 2$, $\lambda_\mu = 1$, $Ca_E = 0.2$: (a) $T = 0$, (b) $T = 6$, (c) $T = 12$, and (d) $T = 18$.

velocity. When the electric conductivity ratio is much smaller than the permittivity ratio, the vortices exist in the nonuniform electric field and are beneficial to droplet migration.

(3) The droplet migrates toward the weaker electric field when $\lambda_\sigma < 1$. In most cases, the electric force acts toward the inside of the droplet. The electric force at the top half

of the droplet is greater than that at the bottom half of the droplet, and a downward electric force is produced. As a result, the droplet migrates toward the weaker electric field. With the increase of permittivity ratio λ_ε, the electric force at the droplet axis poles increases, which is beneficial to the increase of droplet migration velocity. However, the

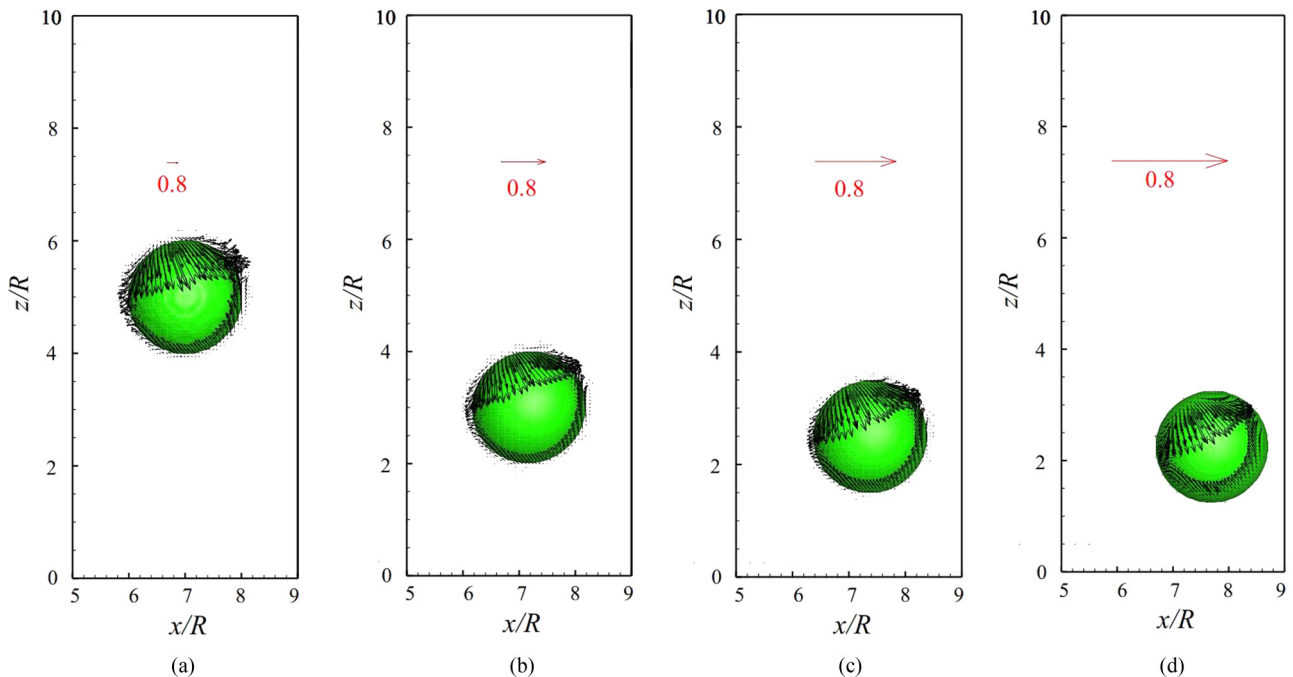FIG. 22. Evolution of droplet positions and corresponding electric force distributions at $y = 5R$ when $\lambda_\sigma = 0.5$, $\lambda_\varepsilon = 2$, $\lambda_\mu = 1$, $Ca_E = 0.2$: (a) $T = 0$, (b) $T = 120$, (c) $T = 240$, and (d) $T = 480$.

appearance of vortices around the droplet hinders migration of the droplet. As a result, the droplet migration velocity has a slight decrease and then increases dramatically with the increase of permittivity ratio λ_ε. Under certain circumstances, the electric force has no fixed direction but a small downward electric force is also produced; the droplet also slowly migrates toward the weaker electric field.

(4) For the droplet in a symmetric nonuniform electric field, the droplet migrates only along one direction. Instead, the droplet in an asymmetric nonuniform electric field tends to experience deformation and dielectrophoretic migration along the normal direction of electric potential profiles. The deformation and dielectrophoretic migration phenomena controlled by a nonuniform electric field has been widely applied to microfluidic devices for droplet separation and transportation. Detailed investigations about effects of electric force and hydrodynamic force on electrohydrodynamic behaviors of a leaky dielectric droplet provide theoretical guidance for the design of appropriate electrode distributions.

ACKNOWLEDGMENTS

[1] V. Pandey, G. Biswas, and A. Dalal, Saturated film boiling at various gravity levels under the influence of electrohydrodynamic forces, Phys. Fluids **29**, 032104 (2017).

[2] Y. Feng, H. Li, K. Guo, X. Lei, and J. Zhao, Numerical study on saturated pool boiling heat transfer in presence of a uniform electric field using lattice Boltzmann method, Int. J. Heat Mass Transf. **135**, 885 (2019).

[3] S. Mhatre, S. Deshmukh, and M. R. Thaokar, Electrocoalescence of a drop pair, Phys. Fluids **27**, 092106 (2015).

[4] C. I. Clark, R. Thakur, and A. R. Abate, Concentric electrodes improve microfluidic droplet sorting, Lab Chip **18**, 710 (2018).

[5] K. Ahn, C. Kerbage, P. T. Hunt, R. M. Westervelt, D. R. Link, and D. A. Weitz, Dielectrophoretic manipulation of drops for high-speed microfluidic sorting devices, Appl. Phys. Lett. **88**, 024104 (2006).

[6] M. Lauricella, S. Melchionna, A. Montessori, D. Pisignano, G. Pontrelli, and S. Succi, Entropic lattice Boltzmann model for charged leaky dielectric multiphase fluids in electrified jets, Phys. Rev. E **97**, 033308 (2018).

[7] G. Taylor, Studies in electrohydrodynamics. I. The circulation produced in a drop by electrical field, Proc. R. Soc. London A **291**, 159 (1966).

[8] A. Esmaeeli and P. Sharifi, Transient electrohydrodynamics of a liquid drop, Phys. Rev. E **84**, 036308 (2011).

[9] J. Zhang, J. D. Zahn, and H. Lin, Transient solution for droplet deformation under electric fields, Phys. Rev. E **87**, 043008 (2013).

[10] S. Torza, G. R. Cox, and G. S. Mason, Electrohydrodynamic deformation and burst of liquid drops, Proc. R. Soc. London A **269**, 295 (1971).

[11] G. Tomar, D. Gerlach, G. Biswas, N. Alleborn, A. Sharma, F. Durst, S. W. J. Welch, and A. Delgado, Two-phase electrohydrodynamic simulations using a volume-of-fluid approach, J. Comput. Phys. **227**, 1267 (2007).

[12] J. Hua, K. L. Lim, and H. C. Wang, Numerical simulation of deformation/motion of a drop suspended in viscous liquids under influence of steady electric fields, Phys. Fluids **20**, 113302 (2008).

[13] Q. Yang, Q. B. Li, and Y. Ding, 3D phase field modeling of electrohydrodynamic multiphase flows, Int. J. Multiphase Flow **57**, 1 (2013).

[14] Y. Lin, Two-phase electro-hydrodynamic flow modeling by a conservative level set model, Electrophoresis **34**, 736 (2013).

[15] Y. Lin, P. Skjetne, and A. Carlson, A phase field model for multiphase electro-hydrodynamic flow, Int. J. Multiphase Flow **45**, 1 (2012).

[16] Y. Cui, N. Wang, and H. Liu, Numerical study of droplet dynamics in a steady electric field using a hybrid lattice Boltzmann and finite volume method, Phys. Fluids **31**, 022105 (2019).

[17] F. P. Salipante and M. P. Vlahovska, Electrohydrodynamics of drops in strong uniform dc electric fields, Phys. Fluids **22**, 112110 (2010).

[18] D. J. Sherwood, Breakup of fluid droplets in electric and magnetic fields, J. Fluid Mech. **188**, 133 (1988).

[19] E. Lac and M. G. Homsy, Axisymmetric deformation and stability of a viscous drop in a steady electric field, J. Fluid Mech. **590**, 239 (2007).

[20] R. J. Melcher and I. G. Taylor, Electrohydrodynamics: A review of the role of interfacial shear stresses, Annu. Rev. Fluid Mech. **1**, 111 (1969).

[21] D. A. Saville, Electrohydrodynamics: The Taylor-Melcher leaky dielectric model, Annu. Rev. Fluid Mech. **29**, 27 (1997).

[22] Q. J. Feng, Dielectrophoresis of a deformable fluid particle in a nonuniform electric field, Phys. Rev. E **54**, 4438 (1996).

[23] D. S. Deshmukh and M. R. Thaokar, Deformation, breakup and motion of a perfect dielectric drop in a quadrupole electric field, Phys. Fluids **24**, 032105 (2012).

[24] D. S. Deshmukh and M. R. Thaokar, Deformation and breakup of a leaky dielectric drop in a quadrupole electric field, J. Fluid Mech. **731**, 713 (2013).

[25] S. Mandal, A. Bandopadhyay, and S. Chakraborty, Effect of surface charge convection and shape deformation on the dielectrophoretic motion of a liquid drop, Phys. Rev. E **93**, 043127 (2016).

[26] S. Mandal, A. Bandopadhyay, and S. Chakraborty, The effect of surface charge convection and shape deformation on the settling velocity of drops in nonuniform electric field, Phys. Fluids **29**, 012101 (2017).

[27] S. Mandal, S. Chakrabarti, and S. Chakraborty, Effect of nonuniform electric field on the electrohydrodynamic motion of a drop in Poiseuille flow, Phys. Fluids **29**, 052006 (2017).

[28] M. S. Lee, J. D. Im, and S. I. Kang, Circulating flows inside a drop under time-periodic nonuniform electric fields, Phys. Fluids **12**, 1899 (2000).

[29] M. R. Thaokar, Dielectrophoresis and deformation of a liquid drop in a non-uniform, axisymmetric AC electric field, Eur. Phys. J. E **35**, 76 (2012).

[30] S. Mhatre and M. R. Thaokar, Drop motion, deformation, and cyclic motion in a non-uniform electric field in the viscous limit, Phys. Fluids **25**, 072105 (2013).

[31] S. Luo, J. Schiffbauer, and T. Luo, Effect of electric field non-uniformity on drops coalescence, Phys. Chem. Chem. Phys. **18**, 29786 (2016).

[32] A. Zhang, Y. Wang, D. Sun, S. Yu, B. Yu, and Y. Li, Development of a VOF+LS+SPP method based on FLUENT for simulating bubble behaviors in the electric field, Numer. Heat Transfer, Part B **71**, 186 (2017).

[33] Y. Wang, D. Sun, A. Zhang, and B. Yu, Numerical simulation of bubble dynamics in the gravitational and uniform electric fields, Numer. Heat Transfer, Part A **71**, 1034 (2017).

[34] U. J. Brackbill, B. D. Kothe, and C. Zemach, A continuum method for modeling surface tension, J. Comput. Phys. **100**, 335 (1992).

[35] L. D. Youngs, Time-dependent multi-material flow with large fluid distortion, in *Numerical Method for Fluid Dynamics*, edited by K. W. Morton and M. J. Baines (Academic Press, New York, 1982), pp. 273–285.

[36] O. Vizika and A. D. Saville, The electrohydrodynamic deformation of drops suspended in liquids in steady and oscillatory electric fields, J. Fluid Mech. **239**, 1 (1992).

[37] Q. J. Feng and C. T. Scott, A computational analysis of electrohydrodynamics of a leaky dielectric drop in an electric field, J. Fluid Mech. **311**, 289 (1996).

[38] D. L. Landau and M. E. Lifshitz, *Electrodynamics of Continuous Media*, 2nd ed. (Pergamon, Oxford, 1975).

[39] B. Nath, G. Biswas, A. Dalal, and K. C. Sahu, Cross-stream migration of drops suspended in Poiseuille flow in the presence of an electric field, Phys. Rev. E **97**, 063106 (2018).